PNAS RESEARCH ARTICLE | CHEMISTRY

Chemically coupling SnO_2 quantum dots and MXene for efficient CO_2 electroreduction to formate and Zn–CO_2 battery

Lili Han[a,b,1,2], Xianyun Peng[c,1], Hsiao-Tsu Wang[d,e,1], Pengfei Ou[f,1], Yuying Mi[g], Chih-Wen Pao[h], Jigang Zhou[i], Jian Wang[i], Xijun Liu[g], Way-Faung Pong[e], Jun Song[f], Zhang Lin[j], Jun Luo[g], and Huolin L. Xin[a,2]

Edited by Yi Cui, Stanford University, Stanford, CA; received April 28, 2022; accepted September 13, 2022

Electrochemical conversion of CO_2 into formate is a promising strategy for mitigating the energy and environmental crisis, but simultaneously achieving high selectivity and activity of electrocatalysts remains challenging. Here, we report low-dimensional SnO_2 quantum dots chemically coupled with ultrathin $Ti_3C_2T_x$ MXene nanosheets (SnO_2/MXene) that boost the CO_2 conversion. The coupling structure is well visualized and verified by high-resolution electron tomography together with nanoscale scanning transmission X-ray microscopy and ptychography imaging. The catalyst achieves a large partial current density of -57.8 mA cm^{-2} and high Faradaic efficiency of 94% for formate formation. Additionally, the SnO_2/MXene cathode shows excellent Zn–CO_2 battery performance, with a maximum power density of 4.28 mW cm^{-2}, an open-circuit voltage of 0.83 V, and superior rechargeability of 60 h. In situ X-ray absorption spectroscopy analysis and first-principles calculations reveal that this remarkable performance is attributed to the unique and stable structure of the SnO_2/MXene, which can significantly reduce the reaction energy of CO_2 hydrogenation to formate by increasing the surface coverage of adsorbed hydrogen.

MXene ultrathin nanosheets | SnO_2 quantum dot | CO_2 reduction reaction | Zn–CO_2 battery

Significance

Electrochemical CO_2 reduction to formate provides an approach to mitigate global warming and simultaneously relieve the growing energy crisis. However, simultaneously achieving desirable catalytic activity and selectivity is greatly limited by the inertness of CO_2 and the sluggish electron transfer kinetics. We report a catalyst with the structure of SnO_2 quantum dots coupled with ultrathin $Ti_3C_2T_x$ MXene nanosheets, which not only can expose more active sites to facilitate the electrical transport but also can construct high-active Sn sites by chemical coupling, offering great opportunities to improve catalytic properties of the CO_2 reduction to formate. This work comprehensively investigates the chemical coupling of the two components that significantly improves their electrocatalytic performances for CO_2 conversion into formate and Zn–CO_2 battery.

Electrochemical conversion of CO_2 into high-value-added fuels has been widely advocated as a promising approach to mitigate the global warming caused by excess emissions of CO_2 and simultaneously relieve the growing energy crisis (1, 2). Particularly, the production of formate (HCOOH) from the CO_2 reduction reaction (CO_2RR) wins much attention because it possesses great prospects in various applications, including formate fuel cells, chemical intermediates, and hydrogen storage systems (53.4 g_{H2} L^{-1} at the normal atmospheric temperature) (3, 4). The electrosynthesis of formate by the two-electron pathway has been demonstrated to be commercially feasible and economically competitive compared to other processes of CO_2RR[4]. Nonetheless, although the overall process is thermodynamically reasonable, the rate of this reaction is often limited by one-electron reduction of CO_2 to form the $CO_2^{\bullet-}$ radical anion, rendering the whole reduction reaction highly inefficient in energy (5, 6). Such limitation seriously hinders the potential of this process for industrial applications. Therefore, there is an urgent need to explore and screen an efficient, cost-effective, and long-life electrocatalyst for the CO_2RR.

Previous studies have reported that several main group metal-based electrocatalysts including Bi (7), Sn (8, 9), Sb (10), and In (11) possess relatively high selectivity for formate production. Among them, Sn-based catalysts have been discovered as a promising candidate in CO_2RR to formate over a broad potential range (12, 13), outperforming most non-precious-metal catalysts, due to their ability to well stabilize the $*CO_2^{\bullet-}$ intermediate and thus facilitate the subsequent activation to formate formation (4, 14, 15). Although it is more attractive compared to other electrodes, the energy efficiency of Sn-based catalysts is too low for practical electrolysis (16, 17), which requires a large overpotential to attain a CO_2 reduction partial current density of 4–5 mA cm^{-2}. To address the intrinsic challenge of Sn-based catalysts for the formate selectivity with large overpotential and low current density, one ideal model of the electrocatalysts could be the hybrid of individual low-dimensional nanomaterial in situ grown on two-dimensional ultra-thin nanostructures, which can expose more active sites, shorten ion diffusion length, and enlarge electrolyte–electrode contact area, thus improving the catalytic activity (18–20). Moreover, the chemical coupling of the two components in a hybrid material also offers great opportunities to improve the catalytic properties through their synergetic effect and adjustment of the electronic structure of active sites (21, 22). However, the fundamental understanding of the chemical coupling interaction in the CO_2RR remains vague.

Here, we coupled low-dimensional SnO_2 quantum dots and ultrathin $Ti_3C_2T_x$ MXene nanosheets (denoted as SnO_2/MXene) for efficient CO_2RR to formate, considering the promising of Sn-based catalysts toward the formate production and the unique properties

Author contributions: L.H., X.P., H.-T.W., P.O., and H.L.X. designed research; L.H., X.P., H.-T.W., P.O., Y.M., C.-W.P., J.Z., J.W., X.L., W.-F.P., and J.S. performed research; X.P., H.-T.W., P.O., J.Z., J.W., W.-F.P., J.S., L.H., and H.L.X. analyzed data; and L.H., X.P., H.-T.W., P.O., Z.L., J.L., and H.L.X. wrote the paper.

The authors declare no competing interest.

This article is a PNAS Direct Submission.

[1]L.H., X.P., H.-T.W., and P.O. contributed equally to this work.

[2]To whom correspondence may be addressed. Email: llhan@fjirsm.ac.cn or huolin.xin@uci.edu.

This article contains supporting information online at http://www.pnas.org/lookup/suppl/doi:10.1073/pnas.2207326119/-/DCSupplemental.

Published October 10, 2022.

of two-dimensional MXene materials (large specific surface area, good hydrophilic surfaces, tuneable termination groups, and high metallic conductivities, etc.) (23). As a result, the obtained SnO_2/MXene catalyst exhibits much higher CO_2RR performance than the mechanical mixture of SnO_2 quantum dots and MXene nanosheets (SnO_2+MXene), such as an enhanced partial current density and significantly improved Faradaic efficiency (FE) of 94% for formate production. In situ X-ray absorption spectroscopy analysis and density functional theory calculations reveal that the excellent performance of SnO_2/MXene catalyst is attributed to its unique and stable structure which reduces the reaction energy of CO_2 protonation by increasing the local coverage of adsorbed hydrogen via promoting water dissociation; meanwhile, it steers the selectivity from HER to CO_2RR-to-HCOOH on MXene. Moreover, the assembled Zn–CO_2 battery based on the SnO_2/MXene cathode exhibited a maximum power density of 4.28 mW cm^{-2}, an open-circuit voltage of 0.83 V, and superior rechargeability.

Results and Discussion

Synthesis and Characterization. The SnO_2/MXene catalyst was prepared by acid-etching and hydrothermal reaction procedures (see Fig. 1*A* and *Methods and Materials* for more details). First, few-layer $Ti_3C_2T_x$ MXene nanosheets were prepared by acid-etching Ti_3AlC_2 MAX phase materials with LiF and HCl. Subsequently, the as-obtained MXene colloid solution was mixed with the Sn precursor ($SnCl_4{\cdot}5H_2O$) suspension, and its pH was adjusted to 8. The mixed solution was subjected to the hydrothermal reaction at 110 °C for 8 h. During the reaction, the nucleated SnO_2 seeds tightly covered the surface of MXene nanosheets and then grew into quantum dots. For comparison, pure SnO_2 was prepared via the same synthetic route above except without the addition of MXene. The SnO_2+MXene composite was prepared by mechanically mixing the as-prepared SnO_2 and MXene with the same mass ratio as that of SnO_2/MXene.

X-ray powder diffraction (XRD) patterns show that the peaks of SnO_2 in SnO_2/MXene exhibit obvious shape broadening (*SI Appendix*, Fig. S1), which is due to the small diameter of the SnO_2 crystallite. The transmission electron microscopy (TEM) image of MXene (*SI Appendix*, Fig. S2) presents that the MXene nanosheets are almost transparent to the electron beam due to their ultrathin thickness. Generally, the ultrathin nanostructures stand out for the large specific area, abundant active sites, and sufficient contact between the electrolyte and the electrode materials, which are favorable to advance the electrochemical performance (24). N_2 sorption of the SnO_2/MXene catalyst displays a type-IV adsorption-desorption isotherms curves with a hysteresis loop, giving a high Brunauer−Emmett−Teller (BET) specific surface area of 94.9 m^2 g^{-1} (*SI Appendix*, Fig. S3). The high surface area is beneficial to the exposure of active sites.

Furthermore, TEM images of SnO_2/MXene (*SI Appendix*, Fig. S4 *A* and *B*) reveal that uniform quantum dots with an average size of 2.78 nm are dispersed on the ultrathin nanosheets. The energy-dispersive X-ray spectroscopy (EDS) elements mapping suggests that the quantum dots are SnO_2 and the nanosheets are MXene (Fig. 1*B* and *SI Appendix*, Fig. S4 *C* and *D*). The corresponding selected area electron diffraction (SAED) pattern in Fig. 1*C* has both polycrystal and monocrystal properties. The monocrystal arrangement of the diffraction spots could be attributed to the hexagonal structure of MXene with $[10\bar{1}0]$ zone axis and the polycrystal diffraction rings could be indexed to the (110), (111), and (200) planes of the rutile SnO_2 phase from the inside out, which are consistent with the XRD results of the coexistence of the MXene and the SnO_2 (*SI Appendix*, Fig. S1). In Fig. 1*D*, the atomic structure of SnO_2 along the [110] zone axis is consistent with the analysis result of the atomic-resolution high-angle annular dark-field scanning transmission electron microscopy (HAADF-STEM) image, which confirms the SnO_2 structure. The result is also evidenced by the high-resolution TEM images (*SI Appendix*, Fig. S4 *E* and *F*). Moreover, the SnO_2 loading on the MXene nanosheets was determined to be 36.7 wt% by inductively coupled plasma optical emission spectrometry analysis.

Furthermore, we performed a three-dimensional (3D) reconstruction analysis for the SnO_2/MXene sample based on a series of HAADF-STEM images at different tilted angles (Fig. 1*E* and *SI Appendix*, Fig. S5). As shown in Fig. 1*E*, the SnO_2 quantum dots are allocated on the MXene substrate in 3D. Importantly, it can be observed from the side view of the 3D structure that these SnO_2 quantum dots are evenly embedded into the interior of the MXene nanosheets (Fig. 1*E* and *SI Appendix*, Fig. S5), indicating that the SnO_2 could have a strong interaction with MXene. By contrast, SnO_2 particles in SnO_2+MXene are unevenly dispersed on the sample and severely aggregated into a larger particle (*SI Appendix*, Fig. S6).

X-ray photoelectron spectroscopy (XPS) and synchrotron-radiation-based X-ray absorption fine spectroscopy (XAFS) was employed to probe the electronic structure and local coordination environment of SnO_2/MXene. As shown in Fig. 1 *F* and *G*, the Sn 3*d* doublet of SnO_2/MXene is shifted by ∼0.5 eV toward lower binding energy relative to that of pure SnO_2 and SnO_2+MXene, whereas the Ti 2*p* doublet of SnO_2/MXene is shifted by ∼0.3 eV toward higher binding energy relative to that of pure MXene. These results indicate possible charge transfer from MXene to SnO_2 upon the formation of the SnO_2/MXene.

The O atom in the SnO_2/MXene catalyst is a key element in electrochemical performance, scanning transmission X-ray microscopy (STXM) and ptychography with nanoscale X-ray absorption spectroscopy (XAS) technique were performed to investigate the electronic structure of O atoms. Fig. 1*H* shows an O *K*-edge STXM-ptychography of the SnO_2/MXene at phase contrast. Together with the STXM-ptychography absorption contrast, it verifies the existence of oxygen-containing species in SnO_2/MXene. To better visualize the oxygen distribution and local bonding environment, chemical imaging by performing the principal component analysis (PCA) of an STXM-ptychography absorption image stack is shown in Fig. 1*I*. The oxygen concentration in the blue region is 10 times lower than that in the yellow and red regions. Therefore, the blue region is MXene dominated while the yellow and red regions have more uniform SnO_2 quantum dots. Fig. 1*J* shows a comparison of O *K*-edge STXM-ptychography XAS at the different areas of the SnO_2/MXene, which can provide further information on the metal-oxygen bonding. The first peak at around 530 eV can be assigned to the t_{2g} peak in Ti–O bonding with a character of O 2*p*-Ti 3*d* hybridization. The second peak at ∼533 eV can be assigned to the e_g state (O 2*p* hybridized with Ti 3*d*) in Ti–O bonding and a_g state (O 2*p* hybridized with Sn 5*s*) in Sn–O bonding. The peak in the blue area at roughly 538 eV could be assigned to Ti–O bonding. The stronger Ti–O signal indicates a stronger Ti–O–Sn covalent bonding in the thinner sample region. The resonance at ∼540 eV corresponds to the transition to O 2*p* hybridized with Ti 4*p* and Sn 5*p* (25, 26). It can be found that the SnO_2/MXene exhibits the mixed chemical states for O. The blue area corresponds to the MXene surface, showing the highest Ti–O t_{2g} but the lowest Sn–O bond, proving that the MXene

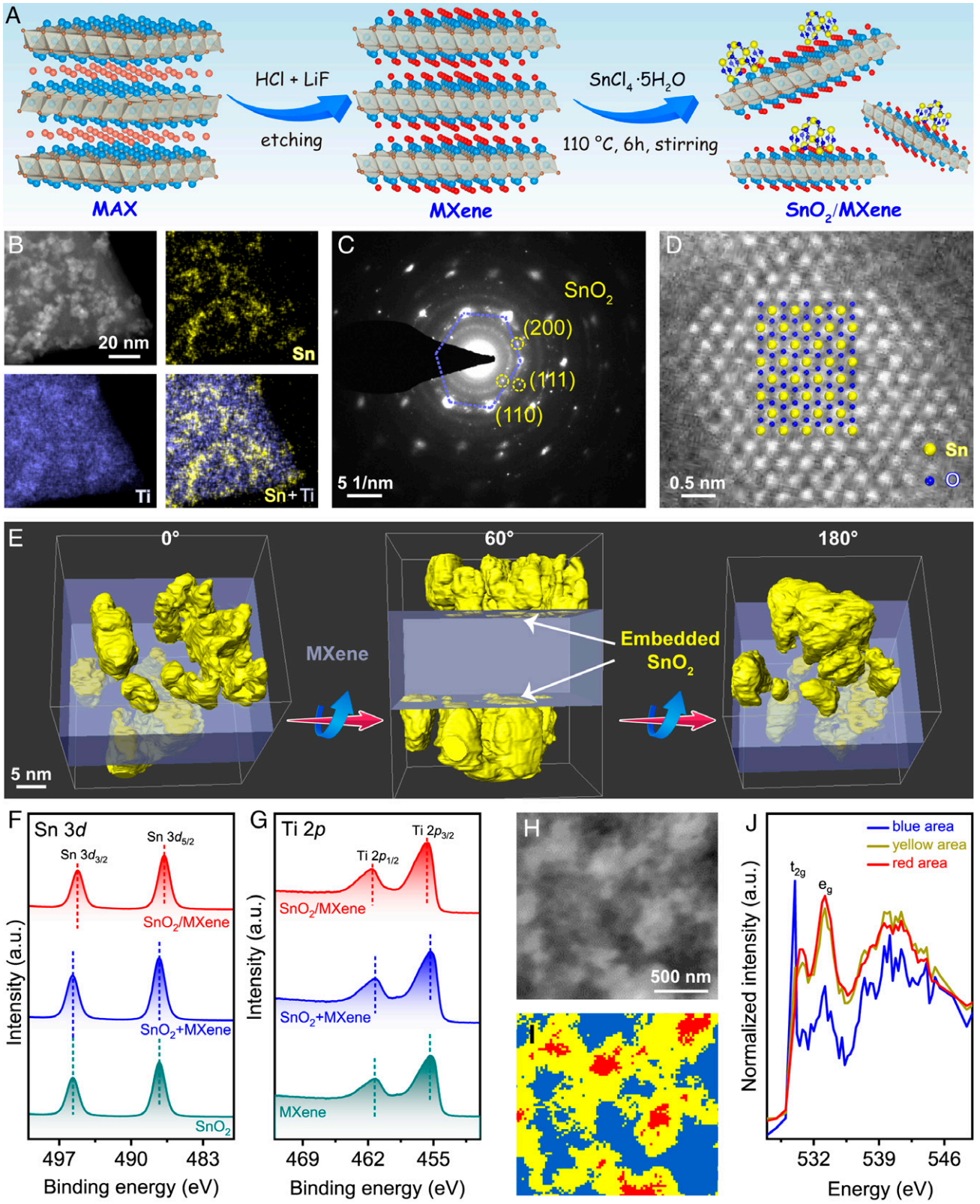

Fig. 1. Fabrication and characterization of SnO_2/MXene. (*A*) Schematic illustration of the fabrication process. (*B*) Low-magnification HAADF-STEM image and the corresponding EDS element images of SnO_2/MXene. (*C*) SAED pattern. (*D*) Atomic-resolution HAADF-STEM image of one SnO_2 quantum dot, and the corresponding atomic structure of SnO_2. (*E*) Volume renderings for SnO_2/MXene at different angles, which derive from experimental results of 3D reconstruction *SI Appendix*, Fig. S5. The yellow and lavender areas represent SnO_2 and MXene, respectively. (*F*) High-resolution Sn 3*d* XPS spectra. (*G*) High-resolution Ti 2*p* XPS spectra. (*H*) STXM-ptychography phase micrograph of the SnO_2/MXene at the O *K*-edge. (*I*) Lateral oxygen concentration distribution over the SnO_2/MXene obtained from the difference of averaged STXM-ptychography absorption micrograph at the O *K*-edge. (*J*) Normalized STXM-ptychography O *K*-edge XANES spectra of selected regions in pristine SnO_2/MXene.

surface is covered by very thin SnO_2. This region can be imagined as the initial growth of SnO_2 on MXene; the strong Ti–O t_{2g} transition and the split Ti–O 4*p* transition (absorption maximum at 537 and 540 eV, respectively) indicate the strong bonding between SnO_2 and MXene through the Ti–O bond. The red and yellow areas have a much enhanced Sn–O bonding feature at

~533 eV and no splitting at 540 eV, which confirms the previous assumption of uniform SnO_2 quantum dots covering these regions. It should be emphasized that Ti–O bonding exists in this region as validated by the 530 eV peak, an indicator of strong Ti–O bonding of SnO_2 onto MXene. This bonding can anchor SnO_2 into MXene and further modify the local electronic structure in SnO_2/MXene. The O local environment difference between freestanding SnO_2 and SnO_2/MXene is present in *SI Appendix*, Fig. S7. The shift of the absorption edge to the lower energy in the hybrid SnO_2/MXene shall correspond to a narrower bandgap and lead to better electric conductivity in SnO_2, an n-type semiconductor.

In addition, the absorption edge position of Sn *K*-edge X-ray absorption near edge structure (XANES) spectrum of SnO_2/MXene in *SI Appendix*, Fig. S8 is located between those of Sn foil (Sn^0) and SnO_2 (Sn^{4+}), which is consistent with the analysis result of XPS. The extended XAFS (EXAFS) spectra in *R*-space and *K*-space (Fig. 1*I* and *SI Appendix*, Fig. S9) for SnO_2/MXene are not the same as those of SnO_2, indicating that the coordination environments of SnO_2 in the SnO_2/MXene are different from those in pure SnO_2. The strong peak at 1.53 Å indicates the existence of Sn–O bonds in SnO_2/MXene, referring to the peaks of Sn–O bonds in SnO_2 (Fig. 1*I*) (27).

CO_2RR Performances. CO_2RR on SnO_2/MXene was performed in a gas-tight H-type cell with a CO_2-saturated 0.1 M $KHCO_3$ solution. Onset potential and current density are significant indicators of the catalytic activity of electrocatalysts. Compared with SnO_2+MXene, SnO_2/MXene exhibits a lower onset potential and higher geometric current density, which indicates superior catalytic activity than that of SnO_2/MXene (Fig. 2*A*). The current density normalized to the BET surface area is shown in *SI Appendix*, Fig. S10. To determine reduction products, potentiostatic electrolysis was conducted on SnO_2/MXene at a few selected potentials between −0.6 and −1.2 V vs. the reversible hydrogen electrode (vs. RHE, all potentials in this work are given vs. RHE unless stated otherwise.). During electrolysis, gaseous products were detected by online gas chromatography (GC), meanwhile, liquid products were monitored by ^1H NMR spectroscopy. The FEs of the products were then derived and summarized in Fig. 2*B* and *SI Appendix*, Fig. S11. As displayed in Fig. 2*B*, formate was first detected over the SnO_2/MXene electrode at −0.6 V with an initial FE of 75%. The selectivity of formate gradually increases and reaches a maximum of 94% at −0.8 V, much higher than that for SnO_2+MXene over the entire potential window and comparable to previously reported state-of-the-art electrocatalysts (*SI Appendix*, Table S1). Moreover, the potential-dependent formate partial current density was also calculated and plotted in Fig. 2*C*. With the applied potential decreased from −0.6 to −1.1 V, the maximum partial current density of −57.8 mA cm^{-2} was achieved.

Electrochemical impedance spectroscopy (EIS) measurement was conducted to gain insight into electrochemical reaction kinetics during the CO_2RR (28). As shown in *SI Appendix*, Fig. S12, the SnO_2/MXene electrode has a lower interfacial charge-transfer resistance than that of SnO_2+MXene. Moreover, the radius of the half-semicircle in the Nyquist plot for SnO_2/MXene is smaller than those of SnO_2+MXene, indicating that SnO_2/MXene owns a much higher charge-transfer rate in the CO_2 reduction process, eventually leading to faster electrochemical reaction kinetics (29). Electrochemical double-layer capacitances (C_{dl}) for these catalysts were also measured to further gain insight into the high CO_2RR activity of SnO_2/MXene. *SI Appendix*, Fig. S13 shows that SnO_2/MXene has a

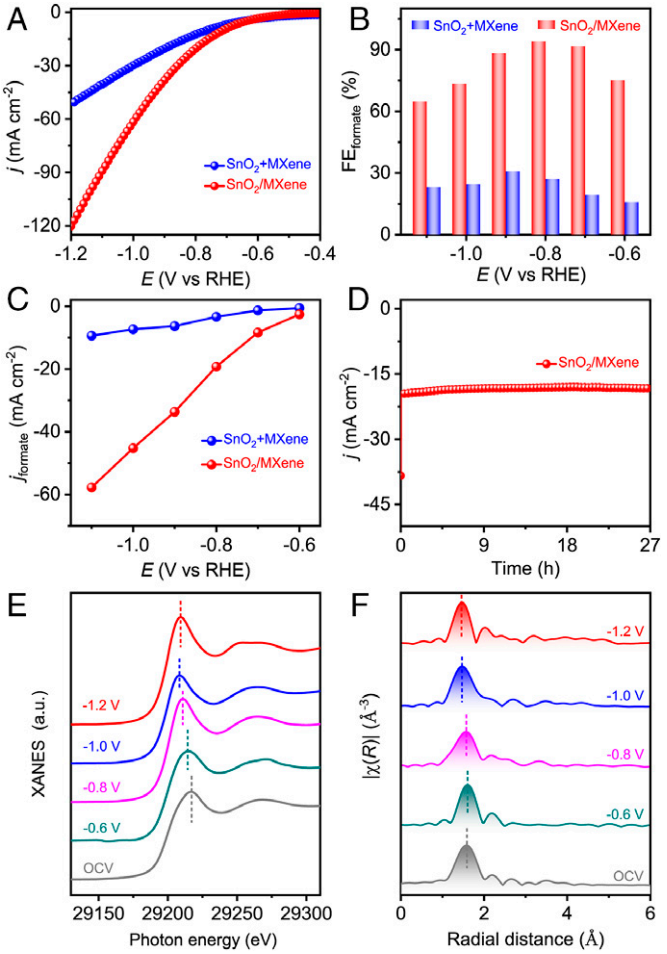

Fig. 2. Electrochemical CO_2 reduction on SnO_2+MXene and SnO_2/MXene in CO_2-saturated 0.1 M $KHCO_3$ aqueous solution. (*A*) LSV curves. (*B*) Potential-dependent FEs of formate. (*C*) Partial current density for formate product. (*D*) Long-term electrocatalytic stability test of SnO_2/MXene. (*E*) In situ normalized XANES profiles of Sn *K*-edge for SnO_2/MXene. (*F*) k^2-weighted Fourier-transformed (FT)-EXAFS spectra corresponding to (*E*).

C_{dl} value of 45.62 mF cm^{-1}, which is much larger than that of SnO_2+MXene (15.42 mF cm^{-1}). This implies higher surface area and more exposed active sites for SnO_2/MXene, which is beneficial to enhancing CO_2RR activity. Moreover, electrocatalytic stability is vital to practical applications. The stability of SnO_2/MXene was evaluated via the electrolysis at −0.8 V for 27 h, where the current density remains negligible degradation over the long-term continuous electrolysis (Fig. 2*D*). The characterization results of SnO_2/MXene after the stability test (*SI Appendix*, Figs. S14 and S15) further confirm the robust electrochemical stability of the SnO_2/MXene catalyst.

To explore the active sites for the high CO_2RR activity (30, 31), we performed in situ XAFS analysis during CO_2RR in a CO_2-saturated 0.1 M $KHCO_3$ aqueous solution to monitor the change of the oxidation states and local chemical environment of Sn species in the SnO_2/MXene. Upon decreasing the applied potentials from −0.6 to −0.9 V, the Sn *K*-edge XANES spectra (Fig. 2*E* and *SI Appendix*, Fig. S16) exhibit a gradual shift toward lower energy. The Sn *K*-edge XANES profiles suggest that the oxidation valence state of the Sn species in SnO_2/MXene is higher than metallic Sn^0 and lower than Sn^{4+}, and the valence decreases with the more negative applied potential. Furthermore, to probe the coordination environment of Sn sites in the SnO_2/MXene catalyst, EXAFS fitting was also performed to extract the structure parameters (Fig. 2*F* and

SI Appendix, Fig. S17 and Table S2). The bond length of Sn–O gradually shortens with the more negative applied potential and the coordination number decreases until at −1.2 V. These results indicate that Sn species in the SnO_2/MXene catalyst experienced a gradual reduction during CO_2RR, which is consistent with previous research results of CO_2RR electrocatalysts (32, 33). Based on the above analysis, it can be concluded that the most favorable CO_2RR active center of the SnO_2/MXene catalyst is the Sn site.

Theoretical Calculations. In the alkaline environment, the protonation of $*CO_2$ requires either the hydrogen adsorbed on the catalyst surface (H_{ad}) or proton directly from H_2O molecules. The breakage of the H–OH bond in H_2O molecules is necessary to provide the proton source for the CO_2RR. Previously, the incorporation of oxides or hydroxides on metal surfaces has been demonstrated to increase H_{ad} coverage by destabilizing H_2O molecules (31, 34, 35), while still maintaining the alkaline pH locally. We hypothesized that the tin oxide or its hydroxide on MXene could enhance the surface coverage of H_{ad}, yet meanwhile allow us to maintain the alkaline environment that favors the CO_2RR and steers the selectivity from HER on MXene to $*CO_2$ protonation. We thus performed density functional theory (DFT) calculations to compare the adsorption and dissociation energy of the H_2O molecule, and the adsorption energy of H_{ad} on $Sn_3O_6H_6$/MXene and MXene (see *Materials and Methods* and *SI Appendix* for details of DFT calculations). The $Sn_3O_6H_6$ system was chosen in our model since the spillover of O atoms in these oxides to form hydroxides is favored in the electrochemical environment (36). As shown in Fig. 3 *A*–*C*, we found that both the energies of H_2O adsorption and dissociation are significantly smaller on $Sn_3O_6H_6$/MXene than those on MXene, whereas the energy of H_{ad} adsorption remains similar, not much affected by the introduction of $Sn_3O_6H_6$ on MXene. As a result, the presence of $Sn_3O_6H_6$ helps facilitate H_2O adsorption and destabilize the H_2O molecules, which is expected to enhance the H_{ad} coverage and maintain the local pH.

To understand the role of increased H_{ad} coverage, we further performed DFT calculations to provide theoretical insights into the selectivity tuning of CO_2RR. The previous studies (15, 37) have shown that the protonation of $*CO_2$ is a key reaction step in branching HCOOH and other C_1 products. The HCOOH pathway was proposed to first have the $*CO_2$ hydrogenated to *OCHO, and *OCHO is then further hydrogenated to generate HCOOH. Other C_1 products undergo the protonation of $*CO_2$ to form *COOH, followed by the removal of OH in *COOH to form *CO. As seen in Fig. 3 *D* and *E*, the surface H_{ad} is confirmed to involve in the protonation of $*CO_2$ to selectively form *OCHO, and thus enhance the activity and selectivity of $Sn_3O_6H_6$/MXene due to an enhanced H_{ad} coverage. This is also evidenced by our DFT calculations where two different mechanisms of protonation on $Sn_3O_6H_6$/MXene were compared (*SI Appendix*, Fig. S18 *A* and *B*). Both the direct proton-electron coupled transfer (PECT) and H-shuttling model (38) (more details can be found for H_{ad} coverage effect in *SI Appendix*) indicate that H_{ad} is more thermodynamically favorable to attack the C atom of adsorbed $*CO_2$ to form *OCHO and then distinguishes the generation of HCOOH from other C_1 products on $Sn_3O_6H_6$/MXene. Meanwhile, HER is more thermodynamically favored on the surface of MXene in SnO_2+MXene, which results from significantly increased reaction energy of $*CO_2$ protonation (Fig. 3 *F* and *G* and *SI Appendix*, Fig. S18 *C* and *D* and Table S3). Collectively, the incorporation of $Sn_3O_6H_6$ on MXene would increase H_{ad}

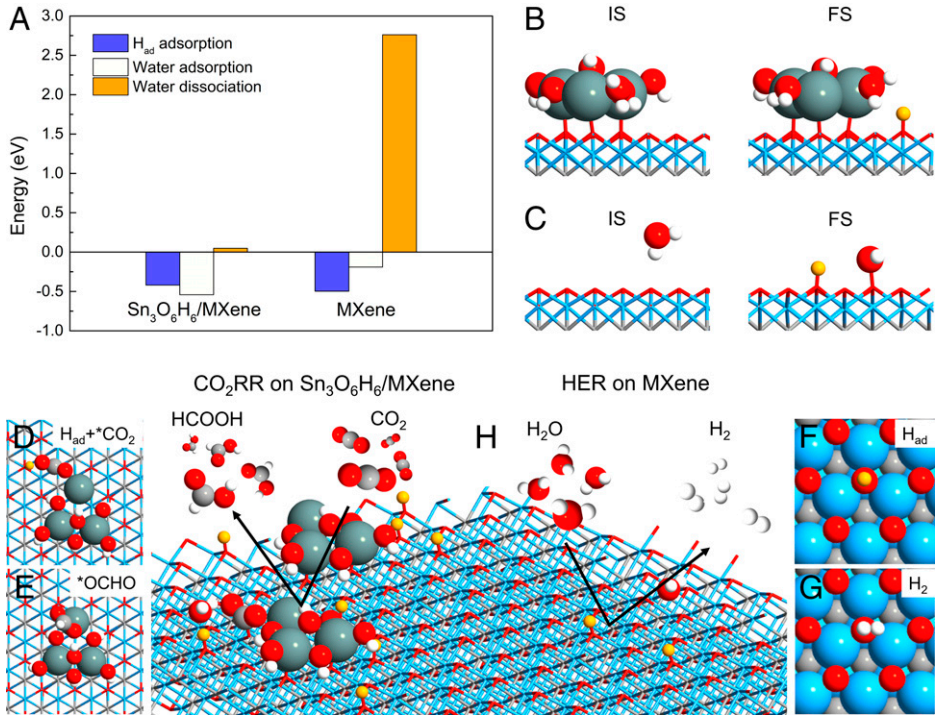

Fig. 3. DFT calculations of water activation, CO_2 reduction reaction, and hydrogen evolution reaction on $Sn_3O_6H_6$/MXene and MXene. (*A*) The calculated energies of H_{ad} adsorption, water absorption, and water dissociation on $Sn_3O_6H_6$/MXene and MXene. The optimized configurations of $*H_2O$ (initial state, IS) and H_{ad}+*OH (final state, FS) on (*B*) $Sn_3O_6H_6$/MXene and (*C*) MXene. Top views of key reaction intermediates, (*D*), H_{ad}+$*CO_2$ and (*E*) *OCHO in CO_2RR-to-HCOOH on $Sn_3O_6H_6$/MXene, as well as (*F*) H_{ad} and (*G*) H_2 in HER on MXene. (*H*) Illustration of selectivity steering from HER to CO_2RR-to-HCOOH on MXene with the presence of $Sn_3O_6H_6$ due to locally increased H_{ad} coverage via destabilizing water molecules. White, gray, red, blue, and celadon balls represent hydrogen, carbon, oxygen, titanium, and tin, respectively, while orange balls represent adsorbed H_{ad} directly from water dissociation. MXene is shown in stick mode in subfigures (*B*–*E*, *H*) to improve visibility.

coverage near the interface and enhance the selectivity of CO_2RR-to-HCOOH on $Sn_3O_6H_6$/MXene (Fig. 3*H*).

Zn–CO_2 Battery. Given the excellent electrochemical CO_2RR performances, the SnO_2/MXene catalyst may have great potential applications in energy conversion devices. For this purpose, we employed the SnO_2/MXene as the cathode and Zn foil as the anode to devise an aqueous rechargeable Zn–CO_2 battery (Fig. 4*A*). A mixed solution of 1 M KOH and 0.02 M $Zn(CH_3COO)_2$ was used as the anodic electrolyte and 0.1 M CO_2-saturated $KHCO_3$ as the cathodic electrolyte. A bipolar membrane for stabilizing different pH values of anolyte and catholyte was applied in opposite directions to enable one device's charging and discharging process. Fig. 4*B* shows that the Zn–CO_2 battery driven by the SnO_2/MXene exhibits a stable open-circuit voltage of 0.83 V for 120 min, which is larger than that of SnO_2+MXene (0.72 V). The charge–discharge polarization curves in Fig. 4*C* depict that a higher discharge current and a smaller discharge–charge voltage gap are accomplished on the SnO_2/MXene-based Zn–CO_2 battery compared to that of the SnO_2+MXene-based one. Specifically, the Zn–CO_2 battery assembled by the SnO_2/MXene CO_2-cathode shows a discharge voltage of 0.53 V at a current density of 2 mA cm^{-2}, whereas the SnO_2+MXene only gives a discharge voltage of 0.25 V. Moreover, the battery driven by the SnO_2/MXene CO_2-cathode exhibits a maximum power density of 4.28 mW cm^{-2} at a current density of 13.57 mA cm^{-2} (Fig. 4*D*), which is 4.26 times larger than that of SnO_2+MXene (0.86 mW cm^{-2}, 5.46 mA cm^{-2}), and surpasses most of other previously reported Zn–CO_2 batteries (Fig. 4*E* and *SI Appendix*, Table S4). Moreover, the FE for formate production from the Zn–CO_2 battery based on the SnO_2/MXene electrode is higher than 85% at the discharge current densities of 5, 7.5, and 10 mA cm^{-2}, (*SI Appendix*, Fig. S19), suggesting the dominance of CO_2-to-formate conversion during the battery discharge. These results demonstrate the higher activity of the SnO_2/MXene catalyst enabling better rechargeability.

To further evaluate the rechargeability of the Zn–CO_2 battery, the cycling rechargeability was further evaluated by cyclic galvanostatic discharge–charge curves recorded by chronopotentiometry at a current density of 2 mA cm^{-2} within 10 min recurrent galvanostatic for SnO_2+MXene and 20 min for SnO_2/MXene (Fig. 4*F*). Remarkably, the battery driven by SnO_2/MXene demonstrates superior cycling stability compared to

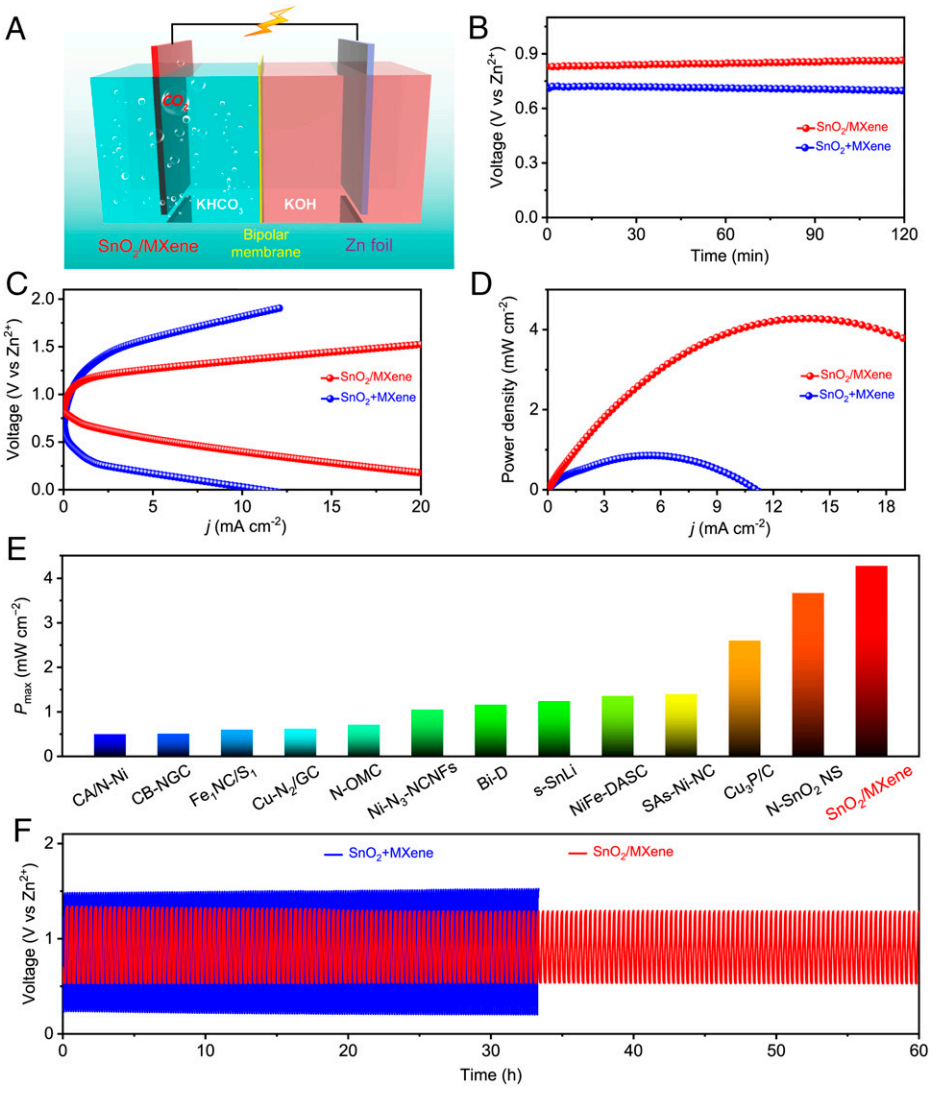

Fig. 4. Rechargeable Zn–CO_2 battery measurements on SnO_2+MXene and SnO_2/MXene cathodes. (*A*) Schematic configuration of Zn–CO_2 battery. (*B*) Open-circuit voltage plots. (*C*) Polarization curves. (*D*) Power density plots corresponding to *C*. (*E*) Comparison of the maximum power densities (P_{max}) of SnO_2/MXene and previously reported electrocatalysts in Zn–CO_2 batteries. (*F*) Galvanostatic discharge–charge cycles plotted against time at 2 mA cm^{-2}.

SnO_2+MXene. For the SnO_2/MXene cathode, the voltage fading is negligible with a stable narrow discharge-recharge voltage gap and a super stable energy efficiency (discharge end voltage divided by charging end voltage) around 41.18% after 60 h continuous testing, reflecting superior rechargeability. Comparatively, the energy efficiency of the battery-driven by the SnO_2+MXene electrode decreases from 15.93 to 14.26%, and the potential gap becomes bigger and bigger with the increase in testing time. The above results verify the promising potential of SnO_2/MXene as the cathode for a long-life rechargeable Zn–CO_2 battery.

Conclusions

In summary, we designed and synthesized low-dimensional SnO_2 quantum dots anchored on ultrathin $Ti_3C_2T_x$ MXene nanosheets for electrochemical CO_2 reduction into formate, which employs its unique and stable structure to reduce the reaction energy of CO_2 hydrogenation to formate by destabilizing the water and the water dissociation to increase the surface coverage of adsorbed hydrogen. The obtained SnO_2/MXene catalyst exhibited a high FE of 94% for formate production at a moderate overpotential. Additionally, the assembled Zn–CO_2 battery based on the SnO_2/MXene cathode exhibited a maximum power density of 4.28 mW cm^{-2} and an open-circuit voltage of 0.83 V as well as superior rechargeability. This work broadens the way toward developing highly efficient electrocatalysts with excellent activity and selectivity for electrochemical CO_2 reduction energy conversion technology and device.

Materials and Methods

Synthesis of SnO_2/MXene. Typically, the SnO_2 quantum dots anchored on the MXene nanosheets were synthesized through an acid-etching and hydrothermal reaction procedure. Typically, 0.2 mmol of tin chloride hydrate ($SnCl_4{\cdot}5H_2O$) was dissolved in 40 mL MXene colloidal solution (1 mg mL^{-1}). After stirring and sonicating separately for 120 min, the pH of the solution was adjusted to 8 with ammonium hydroxide. Subsequently, the resulting solution was continually stirred and degassed under an Ar atmosphere for 60 min. Then, the mixture was transferred to a Teflon-lined stainless-steel autoclave, heated to 110 °C, and maintained at this temperature for 8 h under continuous stirring conditions. After natural cooling to room temperature, the SnO_2/MXene sample was obtained by centrifuging, washing, and freeze-drying. For comparison, pure SnO_2 was also synthesized by the same process above, except that no MXene was added. In addition, the SnO_2+MXene composite was obtained by mechanically mixing the pure SnO_2 suspension with the MXene solution in the same mass ratio of SnO_2 to MXene as that of SnO_2/MXene, followed by the freeze-drying process.

Assembly and Testing of Zn–CO_2 Battery. The aqueous rechargeable Zn–CO_2 battery was constructed in an H-type cell with a double-electrolyte system separated by a bipolar membrane. A polished Zn foil and a carbon cloth (1×1 cm^2) loaded with the catalyst were applied as the anode and cathode, respectively. A mixed solution of 1 M KOH and 0.02 M $Zn(CH_3COO)_2$ was used as the anodic electrolyte to ensure Zn electrochemical reactions at the Zn anode, and 0.1 M CO_2-saturated $KHCO_3$ as the cathodic electrolyte. During the battery tests, CO_2 was controlled by a mass flow meter to continuously flow through the cathode compartment at a rate of 20 standard cubic centimeters per minute. Measurements were performed on CHI 760E electrochemical workstation at room temperature. The open-circuit voltage (OCV) was firstly collected within 120 min. The galvanostatic charge-discharge curves were recorded by chronopotentiometry at a current density of 2 mA cm^{-2} with 10 min per cycle for SnO_2+MXene (5 min charge and 5 min discharge) and 20 min for SnO_2+MXene (10 min charge and 10 min discharge). Both the current density and power density were normalized to the effective surface area of the cathode.

DFT Calculations. Ab-initio DFT calculations were performed using Vienna Ab-initio Simulation Package (VASP) software (39) to study CO_2RR and HER on MXene and SnO_2/MXene. The interaction between the ionic core and valence electrons was described by the projector augmented wave method (40) with a plane wave basis up to an energy cutoff of 450 eV. Considering that saturation of oxygen atoms in the metal clusters was favored under negative applied potentials and aqueous media conditions in CO_2RR, we modeled the SnO_2/MXene interface by depositing a fully hydroxylated tin oxide cluster ($Sn_3O_6H_6$) on a 7-atomic-layer 4×4 O-terminated MXene (0001) surface. The Brillouin zone was sampled by a Gamma-centered $2 \times 2 \times 1$ *k*-point grid generated by the Monkhorst-Pack scheme (41). To avoid periodic interaction, a vacuum region of about 15 Å was used. The zero damping DFT-D3 method of Grimme was also applied to improve the description of weak van der Waals interactions (42). During the geometry optimization, atoms in the bottommost three layers of $Ti_3C_2O_2$ were fixed to their bulk positions, whereas other layers together with the tin oxide cluster and adsorbates on the surface were allowed to relax. Convergency was regarded as achieved for geometry optimization when the Hellman-Feynman force on each ion was smaller than 0.01 eV $Å^{-1}$.

Data, Materials, and Software Availability. All study data are included in the article and/or *SI Appendix*.

ACKNOWLEDGMENTS. This work was supported by the US NSF (CHE-1900401) and the start-up funding of H.L.X. The XAFS spectra obtained from beamline TPS 44A at the National Synchrotron Radiation Research Center are appreciated. STXM-ptychography measurement was performed at the SM beamline of the Canadian Light Source, which is supported by the Canada Foundation for Innovation, the Natural Sciences and Engineering Research Council of Canada, the National Research Council of Canada, the Canadian Institutes of Health Research, the Government of Saskatchewan, and the University of Saskatchewan. X.P., Y.M., X.L., Z.L. and J.L. are unfunded.

Author affiliations: [a]Department of Physics and Astronomy, University of California, Irvine, CA 92697; [b]State Key Laboratory of Structural Chemistry, Fujian Institute of Research on the Structure of Matter, Chinese Academy of Sciences, Fuzhou 350002, China; [c]Institute of Zhejiang University-Quzhou, Quzhou 324000, China; [d]Bachelor's Program in Advanced Materials Science, Tamkang University, New Taipei City 25137, Taiwan; [e]Department of Physics, Tamkang University, New Taipei City 25137, Taiwan; [f]Department of Mining and Materials Engineering, McGill University, Montreal, QC H3A 0C5, Canada; [g]Institute for New Energy Materials & Low-Carbon Technologies and Tianjin Key Lab of Photoelectric Materials & Devices, School of Materials Science and Engineering, Tianjin University of Technology, Tianjin 300384, China; [h]National Synchrotron Radiation Research Center, Hsinchu 30076, Taiwan; [i]Canadian Light Source Inc., University of Saskatchewan, Saskatoon, SK S7N 2V3, Canada; and [j]School of Metallurgy and Environment, Central South University, Changsha 410083, China

1. J. Qiao, Y. Liu, F. Hong, J. Zhang, A review of catalysts for the electroreduction of carbon dioxide to produce low-carbon fuels. *Chem. Soc. Rev.* **43**, 631–675 (2014).
2. S. Gao *et al.*, Partially oxidized atomic cobalt layers for carbon dioxide electroreduction to liquid fuel. *Nature* **529**, 68–71 (2016).
3. D. Mellmann, P. Sponholz, H. Junge, M. Beller, Formic acid as a hydrogen storage material–Development of homogeneous catalysts for selective hydrogen release. *Chem. Soc. Rev.* **45**, 3954–3988 (2016).
4. N. Han, P. Ding, L. He, Y. Li, Y. Li, Promises of main group metal–based nanostructured materials for electrochemical CO_2 reduction to formate. *Adv. Energy Mater.* **10**, 1902338 (2019).
5. X. Lu, D. Y. C. Leung, H. Wang, M. K. H. Leung, J. Xuan, Electrochemical reduction of carbon dioxide to formic acid. *ChemElectroChem* **1**, 836–849 (2014).
6. F. Li *et al.*, Towards a better Sn: Efficient electrocatalytic reduction of CO_2 to formate by Sn/SnS_2 derived from SnS_2 nanosheets. *Nano Energy* **31**, 270–277 (2017).
7. J. Fan *et al.*, Large-area vertically aligned bismuthene nanosheet arrays from galvanic replacement reaction for efficient electrochemical CO_2 conversion. *Adv. Mater.* **33**, e2100910 (2021).
8. S. Liu *et al.*, Efficient electrochemical reduction of CO_2 to HCOOH over sub-2 nm SnO_2 quantum wires with exposed grain boundaries. *Angew. Chem. Int. Ed. Engl.* **58**, 8499–8503 (2019).
9. X. Zheng *et al.*, Sulfur-modulated tin sites enable highly selective electrochemical reduction of CO_2 to formate. *Joule* **1**, 794–805 (2017).
10. J. Medina-Ramos, R. C. Pupillo, T. P. Keane, J. L. DiMeglio, J. Rosenthal, Efficient conversion of CO_2 to CO using tin and other inexpensive and easily prepared post-transition metal catalysts. *J. Am. Chem. Soc.* **137**, 5021–5027 (2015).
11. Y. Huang *et al.*, Size-dependent selectivity of electrochemical CO_2 reduction on converted In_2O_3 nanocrystals. *Angew. Chem. Int. Ed. Engl.* **60**, 15844–15848 (2021).
12. F. Li, L. Chen, G. P. Knowles, D. R. MacFarlane, J. Zhang, Hierarchical mesoporous SnO_2 nanosheets on carbon cloth: A robust and flexible electrocatalyst for CO_2 reduction with high efficiency and selectivity. *Angew. Chem. Int. Ed. Engl.* **56**, 505–509 (2017).
13. L. Fan, Z. Xia, M. Xu, Y. Lu, Z. Li, 1D SnO_2 with wire-in-tube architectures for highly selective electrochemical reduction of CO_2 to C1 products. *Adv. Funct. Mater.* **28**, 1706289 (2018).
14. F. Lei *et al.*, Metallic tin quantum sheets confined in graphene toward high-efficiency carbon dioxide electroreduction. *Nat. Commun.* **7**, 12697 (2016).

15. S. Zhang, P. Kang, T. J. Meyer, Nanostructured tin catalysts for selective electrochemical reduction of carbon dioxide to formate. *J. Am. Chem. Soc.* **136**, 1734–1737 (2014).
16. Y. Hori, H. Wakebe, T. Tsukamoto, O. Koga, Electrocatalytic process of CO selectivity in electrochemical reduction of CO_2 at metal electrodes in aqueous media. *Electrochim. Acta* **39**, 1833–1839 (1994).
17. Y. Chen, M. W. Kanan, Tin oxide dependence of the CO_2 reduction efficiency on tin electrodes and enhanced activity for tin/tin oxide thin-film catalysts. *J. Am. Chem. Soc.* **134**, 1986–1989 (2012).
18. S. Gao *et al.*, Ultrathin Co_3O_4 layers realizing optimized CO_2 electroreduction to formate. *Angew. Chem. Int. Ed. Engl.* **55**, 698–702 (2016).
19. P. Liu, R. Qin, G. Fu, N. Zheng, Surface coordination chemistry of metal nanomaterials. *J. Am. Chem. Soc.* **139**, 2122–2131 (2017).
20. C. Choi *et al.*, Highly active and stable stepped Cu surface for enhanced electrochemical CO_2 reduction to C_2H_4. *Nat. Catal.* **3**, 804–812 (2020).
21. K. Feng *et al.*, $Cu_xCo_{1-x}O$ nanoparticles on graphene oxide as a synergistic catalyst for high-efficiency hydrolysis of ammonia-borane. *Angew. Chem. Int. Ed. Engl.* **55**, 11950–11954 (2016).
22. J. S. Li *et al.*, Coupled molybdenum carbide and reduced graphene oxide electrocatalysts for efficient hydrogen evolution. *Nat. Commun.* **7**, 11204 (2016).
23. A. VahidMohammadi, J. Rosen, Y. Gogotsi, The world of two-dimensional carbides and nitrides (MXenes). *Science* **372**, eabf1581 (2021).
24. C. Tan *et al.*, Recent advances in ultrathin two-dimensional nanomaterials. *Chem. Rev.* **117**, 6225–6331 (2017).
25. J. Zhou, J. Wang, H. Fang, T.-K. Sham, Structural variation and water adsorption of a SnO_2 coated carbon nanotube: A nanoscale chemical imaging study. *J. Mater. Chem.* **21**, 5944–5949 (2011).
26. J. G. Zhou *et al.*, Electronic structure of TiO_2 nanotube arrays from X-ray absorption near edge structure studies. *J. Mater. Chem.* **19**, 6804–6809 (2009).
27. X. Zu *et al.*, Efficient and robust carbon dioxide electroreduction enabled by atomically dispersed $Sn^{\delta+}$ sites. *Adv. Mater.* **31**, e1808135 (2019).
28. X. Song *et al.*, Bifunctional nitrogen and cobalt codoped hollow carbon for electrochemical syngas production. *Adv. Sci. (Weinh.)* **5**, 1800177 (2018).
29. X. Li *et al.*, Exclusive Ni-N_4 sites realize near-unity CO selectivity for electrochemical CO_2 reduction. *J. Am. Chem. Soc.* **139**, 14889–14892 (2017).
30. P. De Luna *et al.*, Catalyst electro-redeposition controls morphology and oxidation state for selective carbon dioxide reduction. *Nat. Catal.* **1**, 103–110 (2018).
31. M. Luo *et al.*, Hydroxide promotes carbon dioxide electroreduction to ethanol on copper via tuning of adsorbed hydrogen. *Nat. Commun.* **10**, 5814 (2019).
32. J. Li *et al.*, Copper adparticle enabled selective electrosynthesis of n-propanol. *Nat. Commun.* **9**, 4614 (2018).
33. Z. Q. Liang *et al.*, Copper-on-nitride enhances the stable electrosynthesis of multi-carbon products from CO_2. *Nat. Commun.* **9**, 3828 (2018).
34. R. Subbaraman *et al.*, Trends in activity for the water electrolyser reactions on 3d M(Ni,Co,Fe,Mn) hydr(oxy)oxide catalysts. *Nat. Mater.* **11**, 550–557 (2012).
35. C.-T. Dinh *et al.*, Multi-site electrocatalysts for hydrogen evolution in neutral media by destabilization of water molecules. *Nat. Energy* **4**, 107–114 (2018).
36. B. Zhou *et al.*, Highly efficient binary copper-iron catalyst for photoelectrochemical carbon dioxide reduction toward methane. *Proc. Natl. Acad. Sci. U.S.A.* **117**, 1330–1338 (2020).
37. Y. Shi *et al.*, Unveiling hydrocerussite as an electrochemically stable active phase for efficient carbon dioxide electroreduction to formate. *Nat. Commun.* **11**, 3415 (2020).
38. X. Nie, M. R. Esopi, M. J. Janik, A. Asthagiri, Selectivity of $CO_{(2)}$ reduction on copper electrodes: The role of the kinetics of elementary steps. *Angew. Chem. Int. Ed. Engl.* **52**, 2459–2462 (2013).
39. G. Kresse, J. Hafner, Ab initio molecular dynamics for liquid metals. *Phys. Rev. B Condens. Matter* **47**, 558–561 (1993).
40. P. E. Blöchl, Projector augmented-wave method. *Phys. Rev. B Condens. Matter* **50**, 17953–17979 (1994).
41. H. J. Monkhorst, J. D. Pack, Special points for Brillouin-zone integrations. *Phys. Rev. B* **13**, 5188–5192 (1976).
42. S. Grimme, J. Antony, S. Ehrlich, H. Krieg, A consistent and accurate ab initio parametrization of density functional dispersion correction (DFT-D) for the 94 elements H-Pu. *J. Chem. Phys.* **132**, 154104 (2010).